Available online at www.sciencedirect.com

SCIENCE DIRECT®

International Journal of Heat and Mass Transfer 47 (2004) 2599–2618

International Journal of HEAT and MASS TRANSFER

www.elsevier.com/locate/ijhmt

Effect of rib orientation and channel rotation on turbulent heat transfer in a two-pass square channel with sharp 180° turns investigated by using large eddy simulation

Akira Murata *, Sadanari Mochizuki

Department of Mechanical Systems Engineering, College of Engineering, Tokyo University of Agriculture and Technology, 2-24-16 Nakacho, Koganei, Tokyo 184-8588, Japan

Received 22 April 2003; received in revised form 19 December 2003

Abstract

Effect of rib orientation and channel rotation on heat transfer in a two-pass square channel with 180° sharp turns was numerically investigated by using the large eddy simulation with a Lagrangian dynamic subgrid-scale model. In the stationary condition, the heat transfer in and after the turn was increased, and it was dominated by the sharp-turn induced flow field. In the rotating condition, the highest rotating speed caused deteriorated heat transfer on the pressure surface of the straight pass. The friction factor was much more sensitive to both the rib arrangement and channel rotation than the heat transfer.

1. Introduction

The effective cooling of a gas turbine rotor blade is essential because the higher efficiency of the turbine requires a higher inlet gas temperature. Generally, this blade cooling is performed by film cooling at the external surface of the turbine blade and also by internal forced-convection cooling which uses winding flow passages inside the turbine blade. In the internal forced-convection cooling, the real phenomena are very complicated due to external forces: the Coriolis force and the buoyancy force in the centrifugal acceleration field. In addition to these external forces, the disturbances induced by turbulence promoters (ribs) and 180° sharp turns further complicate the phenomena [1].

As for the heat transfer in smooth and/or rib-roughened channels with the 180° sharp turn, several researchers investigated the detailed spatial variation of the local heat transfer in the stationary condition with various techniques: wall temperature measurement by using hundreds of thermocouples [2,3], naphthalene sublimation technique to measure the local mass transfer, which was transformed into heat transfer by using the analogy between heat and mass transfer [4,5], unsteady wall temperature measurement by using temperature-sensitive liquid crystal [6,7], and wall temperature measurement by using infrared thermography [8]. In these studies, the characteristic heat transfer variation induced by the ribs and the 180° sharp turn was captured: the high heat transfer areas observed in and after the sharp turn and on and between the ribs. As for the flow field in the stationary condition, the particle image velocimetry technique was applied to the two-pass channel with the 180° sharp turn, and the detailed two-dimensional flow field was measured by Son et al. [9]. For the rotating condition, however, both the flow velocity and wall temperature measurements become very difficult because of the following two reasons: the high centrifugal force preventing the data acquisition system from normal operation and the difficulty in transferring data from the rotating system to the stationary system. Nevertheless, some researchers have

---

[*] Corresponding author. Tel.: +81-42-388-7089; fax: +81-42-385-7204.

E-mail address: murata@mmlab.mech.tuat.ac.jp (A. Murata).

0017-9310/$ - see front matter © 2004 Elsevier Ltd. All rights reserved.
doi:10.1016/j.ijheatmasstransfer.2003.12.016

Nomenclature

$A_{\text{total,nodim}}$	dimensionless total heat transfer area of channel
c_p	specific heat, J/(kg K)
C_S	Smagorinsky constant
C_θ	coefficient of linear component in energy equation $(=A_{\text{total,nodim}}/32)$
D	hydraulic diameter (= side length of straight-pass cross-section), m
e	height of rib, m
f	friction factor $(=\Delta p_{\text{total}}D/(2\rho U_m^2 L))$
F_i	external force term
h	heat transfer coefficient, W/(m^2 K)
j	Colburn's j factor $(=Nu_m/(Re_m Pr^{1/3}))$
K	turn pressure loss coefficient $(=\Delta p_{\text{turn}}/(\frac{1}{2}\rho U_m^2))$
ℓ	length scale $(=0.5D)$, m
L	total duct-axial length of two-pass channel $(=22D)$, m
Nu	Nusselt number $(=hD/\lambda)$
P	rib pitch $(=D)$, m
Δp_{total}	pressure loss between channel inlet and outlet, Pa
Δp_{turn}	pressure loss between turn inlet and outlet, Pa
Pr	Prandtl number $(=0.71)$
Pr_{SGS}	Prandtl number of subgrid-scale model $(=0.5)$
$\dot{q}$	wall heat flux, W/m^2
Re_m	Reynolds number based on bulk mean velocity $(=U_m D/\nu)$
Re_*	Reynolds number based on friction velocity $(=u_*\ell/\nu)$
Ro_m	rotation number based on bulk mean velocity $(=\omega D/U_m)$
Ro_*	rotation number based on friction velocity $(=\omega\ell/u^*)$
S_{ij}	rate-of-strain tensor
St	Stanton number $(=Nu_m/(Re_m Pr))$
t	dimensionless time
T	temperature, K

T_{linear}	linearly increasing component of temperature, K
T_r	friction temperature $(=\dot{q}/(\rho c_p u_*))$, K
u, v, w	dimensionless velocities in x, y, z directions
u_*	mean friction velocity calculated from mean pressure gradient in x direction, m/s
$u_{*\text{mod}}$	mean friction velocity estimated by using bulk mean velocity, m/s
$\overline{u}_m$	dimensionless bulk mean velocity in x direction calculated at the entrance $(=\frac{1}{4}\int_{-1}^{1}\int_{-1}^{1}\overline{u}_{x=0}\,dy\,dz)$
U_m	bulk mean velocity, m/s
x, y, z	dimensionless Cartesian coordinates
$\alpha_{\text{SGS}j}$	subgrid-scale energy flux
Δ_1, Δ_2, Δ_3	grid spacing in ξ, η, ζ directions expressed in (x, y, z) coordinates' scale
η_{eff}	heat transfer efficiency index
λ	thermal conductivity, W/(m K)
ν	kinematic viscosity, m^2/s
ν_{SGS}	dimensionless subgrid-scale eddy viscosity
ω	angular velocity, rad/s
ρ	density, kg/m^3
θ	dimensionless temperature $(=(T-T_{\text{linear}})/T_r)$
$\tau_{\text{SGS}ij}$	subgrid-scale stress tensor
$\tau_{\text{w,s}}$	streamwise component of wall shear stress, Pa
ξ, η, ζ	curvilinear coordinates

Subscripts and superscripts

b	bulk value
B	Blasius
L	local value
m	duct average or based on bulk mean velocity
w	wall
∞	fully developed
*	friction velocity or defined by using u_*
+	dimensionless value based on inner scales
−	grid resolvable component

performed experiments in the rotating condition by measuring the wall temperature distribution using thermocouples for the smooth [10–12] and rib-roughened [13–15] wall two-pass channels with the 180° sharp turn. Liou et al. [16] performed the flow velocity measurement of a rotating two-pass smooth channel with the 180° sharp turn by using the laser Doppler anemometer in addition to the detailed heat transfer measurement by using the transient liquid crystal method. However, it is extremely difficult to perform the experiments in the rotating condition that can identify both the flow structure and its influence on the heat transfer at the same time. Thus, further progress in experimental studies has so far been prevented.

In previous numerical studies of the serpentine flow passage with the 180° sharp turn, the Reynolds-averaged Navier–Stokes equation with a turbulence model was adopted: Banhoff et al. [17] used the k–ε two-equation turbulence model or the Reynolds stress equation model with the wall function, and Lin et al.

[18] used the low-Reynolds number two-equation turbulence model without the wall function. Although this approach using the Reynolds-averaged turbulence model could reproduce the heat transfer of blade cooling to a certain extent, even the Reynolds stress equation model has empirical constants and functions, and therefore the applicability of the model should carefully be examined. Recent advancement in computers enables us to numerically simulate the fluctuating components of the turbulent flow by using the large eddy simulation (LES) or the direct numerical simulation (DNS), and the techniques were applied to the smooth straight duct in the stationary [19–21] and rotating [22,23] conditions. Because LES and DNS directly resolve temporal variation of the fluctuating components, the results are more universal, in other words, more free from the empirical modeling than the Reynolds-averaged turbulence models. Although LES also has empirical constants and functions, the modeling of the turbulence is confined to the subgrid-scale turbulence, and therefore the effect of the empirical modeling on the result is ideally less than that in the Reynolds stress equation model. Recently, the authors performed the numerical analyses by using a dynamic subgrid-scale model for a rotating angled-rib-roughened straight duct [24,25]. Very recently, the authors further performed the LES for a rotating two-pass smooth channel with the 180° sharp turns using parallel computing technique [26], and the effect of the sharp turn and the interaction between the sharp-turn induced and Coriolis-induced secondary flows were examined. However, so far the effect of the rib-induced secondary flow with its possible interaction with the sharp-turn induced and Coriolis-induced secondary flows on the heat transfer has not been investigated by using either LES or DNS.

This study examines how the secondary flows induced by the ribs, the 180° sharp turn, and the Coriolis force interact to each other and how it affects the heat transfer. The large eddy simulation of a very large computational domain was made possible by adopting the parallel computing technique, and it was performed on a supercomputer of massive parallel processors for both stationary and rotating conditions with three different rib arrangements: a 90° transverse rib and two angled 60° rib arrangements.

2. Numerical analysis

Fig. 1 shows the computational domain and coordinate system used in this study. The duct had a square cross-section with a side length of D. The coordinate system was fixed to a rotating channel that had an angular velocity of ω with respect to the axis of rotation parallel to the x-axis. The axial direction of the channel straight pass was parallel to the z direction; the x and y directions were the parallel and perpendicular directions, respectively, to leading/trailing walls. In this study, the side walls were referred to the leading and trailing walls whether the channel rotated or not. The inner and outer walls at the turn A was named the inner and outer walls, respectively. Therefore, it should be noted that "inner wall" and "outer wall" of this study came to the outer and inner sides at the turn B, respectively, although the discussion of this study was for the turn A unless otherwise mentioned. Round-type ribs as used in [17,18] were installed with the in-line arrangement on the trailing and leading walls with the rib angle of 90° or 60° with respect to duct axis of the straight pass. As shown in Fig. 1, the cross-section of the round-type rib was composed of the quadrants of which radius was 0.05D,

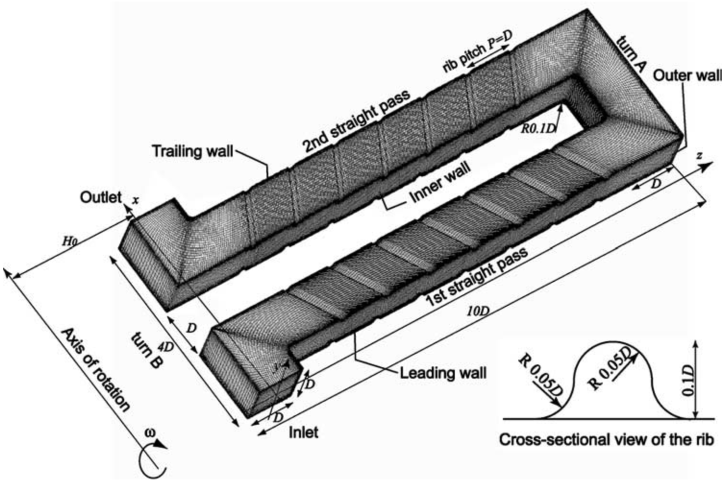

Fig. 1. Schematic of a rotating two-pass rib-roughened square channel with sharp 180° turns (60° rib with NP arrangement is shown).

and thus the rib height was $e = 0.1D$. The streamwise rib-pitch, P, was set equal to the hydraulic diameter, D. This rib arrangement gave the rib height-to-hydraulic diameter ratio $e/D = 0.1$ and the rib pitch-to-rib height ratio $P/e = 10$. This rib arrangement was chosen because it was within the previously reported optimal range for straight ducts considering both the Nusselt number and the friction factor [27–29]. The rib angle, 60°, was chosen as the angle which gave the maximum heat transfer for straight ducts in Han et al. [30]. As shown in Fig. 2, three rib arrangements were investigated in this study: a 90° rib arrangement and two 60° rib arrangements. For the 60° rib "NP" and "PN" arrangements, "N" and "P" were from "Negative" and "Positive" considering relation between angled-rib induced and sharp-turn induced secondary flow directions. For example, in the "PN" arrangement the angled-rib induced secondary flow in the first straight pass circulated in the same direction as the turn A induced one, and on the other hand that in the second straight pass circulated in the opposite direction to the turn A induced one.

The present procedure of the numerical analysis was the same as our recent study [26]. After applying a filtering operation to the incompressible Navier–Stokes equation with a filter width equal to the grid spacing [21], the dimensionless governing equations scaled by a length scale, ℓ $(=0.5D)$, and mean friction velocity, u_*, became a set of dimensionless governing equations with respect to grid resolvable components indicated by overbars as $(\overline{u}, \overline{v}, \overline{w})$ under the assumption of constant fluid properties. In order to simulate a fully developed situation, the pressure and temperature fields were decomposed into the steady and x-directional linear component and the remaining component [31]. By this decomposition, the latter component of the pressure and temperature fields can be treated using a periodic boundary condition in the x direction. As shown in Eq. (1), F_i is an external force term including the Coriolis force, and the buoyancy term was ignored in this study. The mean pressure gradient term (with a value of 2) was added to the external force term as follows:

$$F_i = \begin{pmatrix} 2 \\ 2Ro_*\overline{w} \\ -2Ro_*\overline{v} \end{pmatrix}. \tag{1}$$

In this study, the friction velocity, u_*, was calculated from the force balance between the mean pressure gradient in the x direction and the wall shear stress as follows:

$$\rho u_*^2 = \frac{\ell}{2}\left|\frac{\mathrm{d}p}{\mathrm{d}x}\right|_{m,\mathrm{dim}}. \tag{2}$$

Here, the mean pressure gradient with the subscript, "dim", meant the value with dimension, and it drove the flow in the x direction. By non-dimensionalizing Eq. (2), the dimensionless mean pressure gradient value of 2 came out. Because of the constant mean pressure gradient, the flow rate varied depending on the conditions (the rotation number and the rib arrangement); therefore, the flow rate was not known a priori, and it was calculated from the resultant computed flow field after the fully developed condition was attained.

The temperature was made dimensionless by using a linearly increasing component of temperature, T_{linear}, and a friction temperature, T_r, as $\theta = (T - T_{\mathrm{linear}})/T_r$. Accordingly, the dimensionless energy equation was derived for the grid resolvable component, $\overline{\theta}$. The governing equations in the Cartesian coordinates (x, y, z) were transformed into generalized curvilinear coordinates (ξ, η, ζ) that were aligned to the structured grid coordinate of this study: ζ was the duct-axial direction. The governing equations in the curvilinear coordinate system were expressed as follows [32]:

$$\frac{1}{J}\frac{\partial J\overline{U}^j}{\partial \xi^j} = 0, \tag{3}$$

$$\frac{\partial \overline{u}_i}{\partial t} = -\overline{U}^j\frac{\partial \overline{u}_i}{\partial \xi^j} - \frac{\partial \xi^j}{\partial x_i}\frac{\partial \overline{p}}{\partial \xi^j} + \frac{1}{Re_*}\frac{\partial \xi^j}{\partial x_\ell}\frac{\partial}{\partial \xi^j}\left(\frac{\partial \xi^k}{\partial x_\ell}\frac{\partial \overline{u}_i}{\partial \xi^k}\right) + \frac{\partial \xi^k}{\partial x_j}\frac{\partial \tau_{\mathrm{SGS}ij}}{\partial \xi^k} + F_i, \tag{4}$$

$$\frac{\partial \overline{\theta}}{\partial t} = -\overline{U}^j\frac{\partial \overline{\theta}}{\partial \xi^j} - C_\theta\frac{\overline{u}}{\overline{u}_{\mathrm{m}}} + \frac{1}{Re_*Pr}\frac{\partial \xi^j}{\partial x_\ell}\frac{\partial}{\partial \xi^j}\left(\frac{\partial \xi^k}{\partial x_\ell}\frac{\partial \overline{\theta}}{\partial \xi^k}\right) + \frac{\partial \xi^k}{\partial x_j}\frac{\partial \alpha_{\mathrm{SGS}j}}{\partial \xi^k}, \tag{5}$$

where, $\overline{U}^j$ was a contravariant component of velocity, and the following expressions were assumed: $J = \partial(x,y,z)/\partial(\xi,\eta,\zeta)$, $(x_1, x_2, x_3) = (x, y, z)$, and $(\xi^1, \xi^2, \xi^3) = (\xi, \eta, \zeta)$. In Eq. (5), C_θ of which value was shown in the

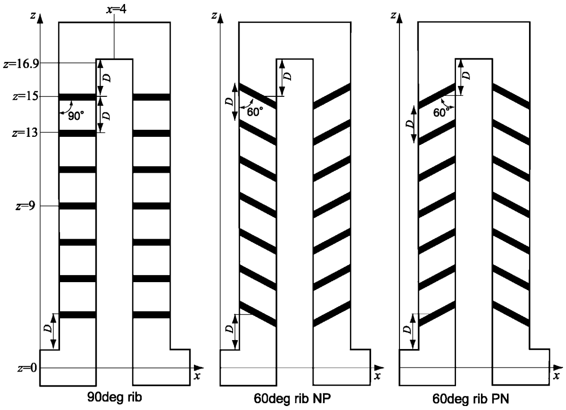

Fig. 2. Rib arrangements of this study (all cases are in-line arrangement).

nomenclature appeared as a result of the energy balance between the temperature increase of the fluid and the heat input through the channel walls.

Subgrid-scale components of stress, $\tau_{\mathrm{SGS}ij}$, and energy flux, $\alpha_{\mathrm{SGS}j}$, were expressed as follows:

$$\tau_{\mathrm{SGS}ij} = 2\nu_{\mathrm{SGS}}\overline{S}_{ij} \tag{6}$$

$$\alpha_{\mathrm{SGS}j} = \frac{\nu_{\mathrm{SGS}}}{Pr_{\mathrm{SGS}}}\frac{\partial\xi^k}{\partial x_j}\frac{\partial\overline{\theta}}{\partial\xi^k}, \tag{7}$$

where,

$$\overline{S}_{ij} = \frac{1}{2}\left(\frac{\partial\xi^k}{\partial x_j}\frac{\partial\overline{u}_i}{\partial\xi^k} + \frac{\partial\xi^k}{\partial x_i}\frac{\partial\overline{u}_j}{\partial\xi^k}\right), \tag{8}$$

$$\nu_{\mathrm{SGS}} = C_{\mathrm{S}}^2(\Delta_1\Delta_2\Delta_3)^{2/3}\sqrt{2\overline{S}_{ij}\overline{S}_{ij}}. \tag{9}$$

Because the flow field of this study has no homogeneous direction, we adopted the Lagrangian dynamic subgrid-scale model of Meneveau et al. [33] that averaged the value of C_{S} along the path-line for a certain distance. As for the coefficient of the Lagrangian averaging time scale, the same value of 1.5 as that in [33] was used. The turbulent Prandtl number for the subgrid-scale component, Pr_{SGS}, was set to 0.5 [34]. The width of the test filter was double the grid spacing.

Discretization was performed by a finite difference method using the collocated grid system [32]. The spatial and temporal discretization schemes were similar to those of Gavrilakis [20]: the second order central differencing method and the Crank–Nicolson method for the viscous term, and the second order differencing method satisfying the conservative property [32] and the second order Adams–Bashforth method for the convective term. The external force term was also treated by the second order Adams–Bashforth method. The pressure field was treated following the MAC method [35]. At the wall boundary, no-slip and constant heat flux conditions were imposed. The boundary conditions of the intermediate velocities and the pressure were set following the procedure of [36,37].

The local Nusselt number, Nu_{L}, was calculated from the wall temperature as follows:

$$Nu_{\mathrm{L}} = \frac{2Re_*Pr}{\overline{\theta}_{\mathrm{w}} - \overline{\theta}_{\mathrm{b}}}. \tag{10}$$

The averaged Nusselt number was calculated by using the integrally averaged temperature difference for the area in question.

As explained above, the bulk mean Reynolds number, Re_{m}, varied depending on the conditions (the rotation number and the rib arrangement). In order to maintain turbulent flow for the higher rotation number cases, the value of $Re_*(= u_*\ell/\nu)$ was increased from 1000 to 1500 for $Ro_*(= \omega\ell/u_*)$ of 2. The present combinations of (Re_*, Ro_*) were (1000, 0), (1000, 1), and (1500, 2). The conversion of the dimensionless numbers of this study (Re_*, Ro_*) defined by the mean friction velocity and the length scale, $0.5D$, into those of $(Re_{\mathrm{m}}, Ro_{\mathrm{m}})$ defined by the bulk mean velocity and the hydraulic diameter, D, was summarized in Table 1. In the real aircraft gas turbine engines, the central region of the operating range is in the order of $Re_{\mathrm{m}} \sim 10^4$ and $Ro_{\mathrm{m}} \sim 10^{-1}$ [11]. Note that as compared to the real situation the values of this study are smaller for Re_{m} because of the limited grid resolution and larger for Ro_{m}.

As shown in Fig. 1, the structured grid system was generated by using Gridgen Ver.14 (Pointwise Inc.). The

Table 1
Dimensionless number range of this study and the duct averaged values of f and Nu_{m} (the values in the second line are for higher grid resolution of 71×71 in the duct cross-section with reduced sample size of 30,000 and 40,000 steps for $Ro_* = 1$ and 2, respectively; the smooth channel data are from Murata and Mochizuki [26])

Rib arrangement	Re_*	Ro_*	Re_{m}	Ro_{m}	f/f_{B}	$Nu_{\mathrm{m}}/Nu_\infty(= j/j_\infty)$
90°	1000	0	4680	0	6.95	2.40
	1000	1	3339	1.20	12.55 (+80.6%)	2.62 (+9.2%)
	1500	2	3671	3.27	23.93 (+244%)	2.72 (+13.3%)
60° NP	1000	0	4357	0	7.88	2.63
	1000	1	3447	1.16	11.87 (+50.6%)	2.67 (+1.5%)
			(3505)	(1.14)	(11.53 (+46.3%))	(2.71 (+3.0%))
	1500	2	3772	3.18	22.82 (+190%)	2.77 (+ 5.3%)
			(3728)	(3.22)	(23.29 (+196%))	(2.77 (+5.3%))
60° PN	1000	0	5120	0	5.94	2.43
	1000	1	3437	1.16	11.94 (+101%)	2.68 (+10.3%)
	1500	2	3695	3.25	23.66 (+298%)	2.80 (+15.2%)
Smooth [26]	700	0	4099	0	4.30	1.93
	1000	1	4028	0.99	9.04 (+110%)	2.39 (+23.8%)
	1500	2	3926	3.06	21.28 (+395%)	2.77 (+43.5%)

grids in the physical domain were contracted to the walls and the corners. On the rib-roughened surfaces, the grids were aligned to the ribs. The grid number was mainly $47\times47\times965$ in ξ, η, ζ directions, and this grid configuration, for example, gave a grid spacing of $\Delta_1^+ = 0.39$–17.1, $\Delta_2^+ = 0.51$–12.4, and $\Delta_3^+ = 1.5$–21.8 for the stationary 60° rib NP case. Here, the inner length scale of $\nu/u_{*\mathrm{mod}}$ was used, because the friction velocity, u_*, defined in Eq. (2) overestimated the value. In Eq. (2), the streamwise direction was assumed to be only in the x direction, and therefore it cannot account for the longer total flow distance caused by the change of the streamwise direction in the two-pass channel. In order to estimate appropriate inner length and time scales, the friction velocity, $u_{*\mathrm{mod}}$, was calculated by using the resultant flow rate for each condition and the Blasius equation. For $Ro_* = 2$, higher grid resolution of $47\times47\times1207$ in the ζ direction (grid number was doubled only in the turn section) was adopted because slight oscillation of the flow field was observed in the $47\times47\times965$ grid results. The effect of the grid spacing on the computed result was checked by increasing the grid number to $71\times71\times965$ (or $71\times71\times1207$) for several cases, and no major difference was observed as shown in Table 1. The time step interval was $\Delta t = 1.0\times10^{-4}$, which can be expressed as $\Delta t^+ = 0.015$ when made dimensionless by an inner time scale, $\nu/u_{*\mathrm{mod}}^2$ for the stationary 60° rib NP case.

In order to deal with the very high computational load of this study, the computational domain was decomposed into 64 subdomains in the duct-axial (ζ) direction, and the parallel computing technique was applied. Each subdomain's computation was performed on a different CPU on HITACHI SR8000/MPP (Information Technology Center, The University of Tokyo). When the algebraic equation for each variable was solved by using the SOR method, the values at the subdomain boundaries were transferred to the neighboring subdomains by using MPI functions in each iteration.

The computation was started using the result of the similar condition as an initial condition. At first, the calculations were carried out till the statistically steady flow condition was attained. After that, additional 90,000 steps ($t = 9$ or $t^+ = 1,350$ (60° rib NP)) were performed for computing the statistical values. This 90,000 step computation needed about 11.5×64 CPU hours for the $47\times47\times965$ grid configuration.

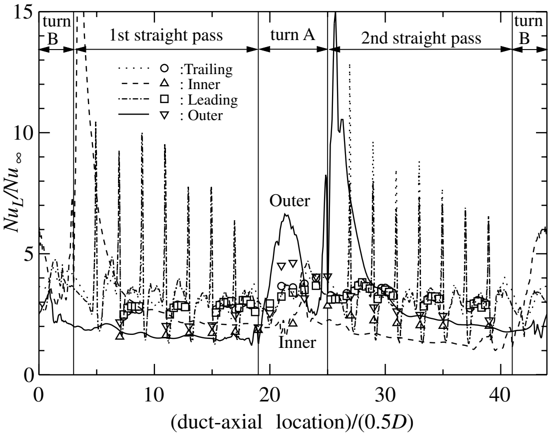

(a) 90deg rib

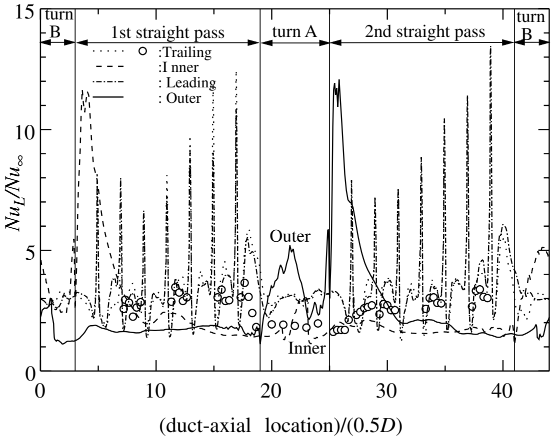

(b) 60deg rib PN arrangement

Fig. 3. Duct-axial variation of local Nusselt number at transverse center ($Re_* = 1000$, $Re_\mathrm{m} =$ (a) 4680 and (b) 5120, $Ro_* = 0$; experimental results [3] (symbols) in (a) and (b) are for $Re_\mathrm{m} = 5000$ and 30,000, respectively, for the same sharp turn geometry with square ribs).

3. Results and discussion

Fig. 3 shows the duct-axial variation of the local Nusselt number at the transverse center. The Nusselt number of this study was normalized using the following empirical correlation for a fully developed pipe flow [38]:

$$Nu_\infty = 0.022 Re_\mathrm{m}^{0.8} Pr^{0.5} \tag{11}$$

The symbols in the figure are the experimental results [3] for the same sharp turn geometry and the same rib arrangement, although the followings differ from the numerical condition: the square cross-section ribs, only one turn with the fully developed inflow condition, and $Re_\mathrm{m} = 30,000$ for the 60° rib PN case (Fig. 3(b)). In spite of the fully-developed inflow condition in the experiments, the installation of the ribs forms a periodic profile in a short distance, and even in the first straight pass the agreement between the numerical and experimental results is good. In the turn, the outer wall gives the highest value, and its variation is also large; however the experimental results show the smaller variation in Fig.

3(a). The Nusselt number on the rib surface of the numerical result is very high as reported in the previous experiments [28].

Figs. 4–6 show the stationary results of the local Nusselt number (a) and the streamwise component of the wall shear stress (b) on all four walls by viewing the flow channel from six different directions. It should be noted that the lower part of "Outer wall" in the figure shows the inner wall values because it is visible through the inlet and outlet of the channel. In (b), zero shear stress boundary is indicated by a white line. In the calculation of the streamwise component of the wall share stress, the streamwise direction was approximated by the ζ direction. In all the three cases of (a), the Nusselt number increases in and after the turn. As was seen in Fig. 3, the outer wall gives two peaks: one is at the middle of the outer end wall and the other is at the second outer corner in the turn. On the side walls (the leading and trailing walls in the figure), the high Nusselt number areas appear at the turn middle and outlet, and those are shifted to the outer wall. These Nusselt

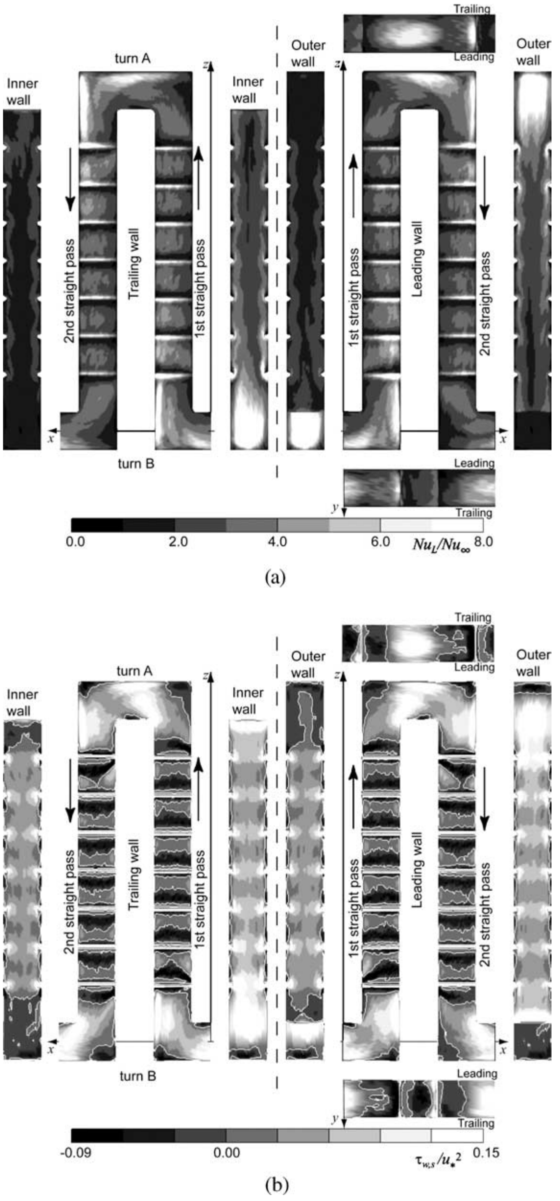

Fig. 4. Time-averaged profiles of (a) Nusselt number and (b) streamwise component of wall shear stress (90° rib, $Re_* = 1000$, $Re_m = 4680$, and $Ro_* = 0$).

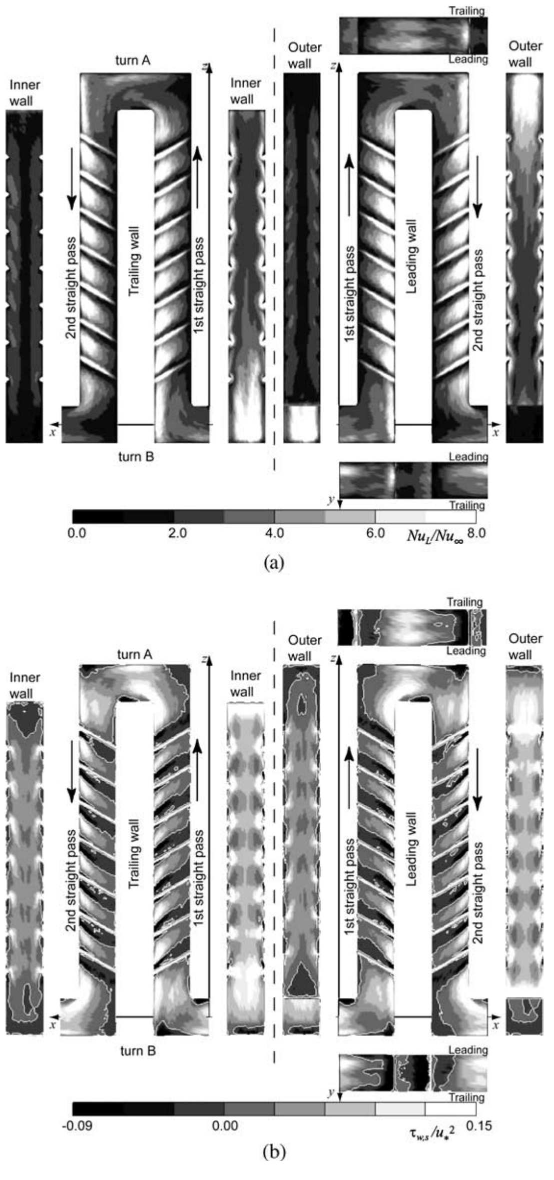

Fig. 5. Time-averaged profiles of (a) Nusselt number and (b) streamwise component of wall shear stress (60° rib NP, $Re_* = 1000$, $Re_m = 4357$, and $Ro_* = 0$).

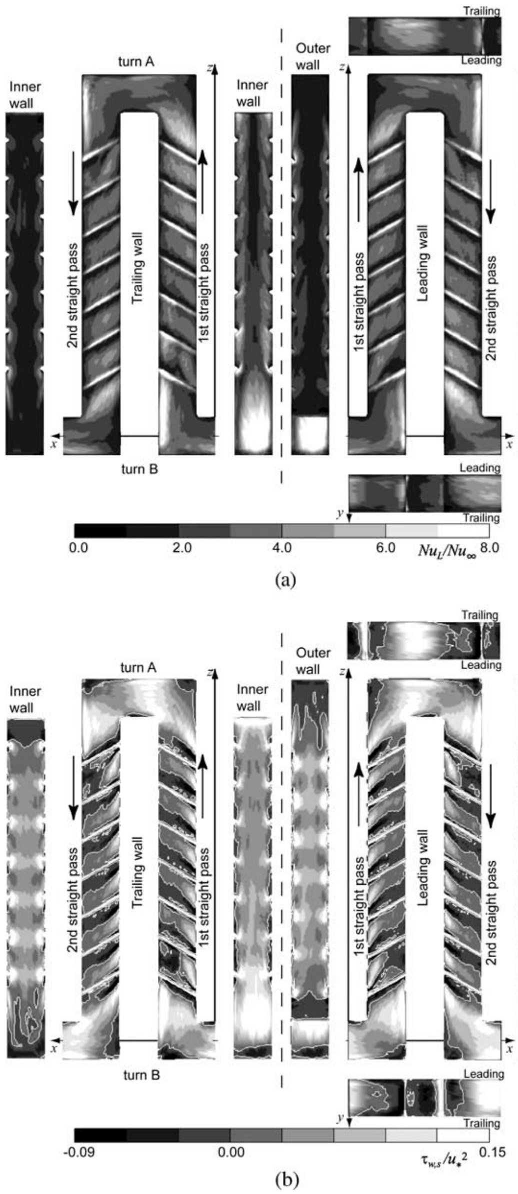

Fig. 6. Time-averaged profiles of (a) Nusselt number and (b) streamwise component of wall shear stress (60° rib PN, $Re_* = 1000$, $Re_m = 5120$, and $Ro_* = 0$).

number variations have also been observed in the previous experiments [5–8]. The flow impingement is confirmed by the high shear stress region in (b) on the outer end wall in the turn and on the outer wall after the turn. The low heat transfer on the inner wall is attributed to the flow separation, and it is also confirmed by the negative shear stress on the inner wall in and after the turn. When the two outer corner regions are examined, both are covered by the negative shear stress and therefore the existence of the flow separation is confirmed. In the second outer corner region, the high heat transfer is correlated with the negative wall shear stress. At the entrance of the turn, the shear stress on the inner and leading/trailing walls becomes high, but this region does not show the high heat transfer because it is covered by the high temperature fluid. These characteristics in and around the turn are qualitatively similar to the smooth two-pass channel case of [26]. In the rib-roughened straight pass, the periodic rib installation establishes the periodic profiles in a few rib-pitches after the turn. When the 60° rib NP and PN arrangements are compared in Figs. 5 and 6, the NP arrangement (Fig. 5) shows the higher Nusselt number on the rib-roughened walls, and the reason will be explained below.

Figs. 7–9 show the time-averaged velocity vectors in the plane normal to the local duct-axis and the isocontours of the time-averaged plane-normal velocity component ($\overline{u}$ or $\overline{w}$) and temperature, $\overline{\theta}$, for the stationary condition. In the figure, the values at five different duct-axial locations in and around the turn A are shown: from top to bottom $x = 4$ (mid-plane in the turn), $z = 16.9$, 15, 13, and 9 (note that $z = 17$ and 9 correspond to the tip of the inner wall and the middle of the straight pass, respectively, and z is normalized by using $\ell = 0.5D$). It should be noted that the scale of the velocity vectors for $z = 13$ and 9 in Figs. 7 and 9 is different from the rest in order to magnify the weaker secondary flow. At the entrance of the turn ($1 < x < 3$ of the second figures from top), the flow is accelerated to the inner wall side, and the high streamwise velocity region is shifted toward the inner wall, although the temperature profile does not change that much at the same location. The tendency is very clearly seen in the 90° rib case of Fig. 7. This dissimilarity between $\overline{w}$ and $\overline{\theta}$ is the reason for the high wall shear stress near the inner wall corner without the heat transfer augmentation seen in Figs. 4–6. In the mid-plane of the turn (see top-middle figures), the flow separation is observed near the inner wall as a reverse flow region. For the 90° rib (Fig. 7) and the 60° rib NP (Fig. 8), after the turn, the peaks of both $\overline{w}$ and $\overline{\theta}$ are shifted to the outer wall, and it lasts for a long distance. On the other hand, for the 60° rib PN (Fig. 9), the peaks of $\overline{w}$ and $\overline{\theta}$ once shifted to the outer wall move back toward the inner wall and at $z = 9$ they come to duct center, because the angled-rib induced vortex pair forms a return flow at $y = 0$ and the peaks of $\overline{w}$ and $\overline{\theta}$ are shifted to the angled-rib leeward side [24], which corresponds to the inner wall side in the second straight pass of the PN arrangement. In other words, the PN arrangement has to redevelop the secondary flow suitable for the rib orientation after the turn, and this is the reason for the lower Nusselt number on the rib-roughened surface than the NP arrangement as seen in Figs. 5 and 6.

The local Nusselt number and the streamwise component of the wall shear stress for the rotating conditions

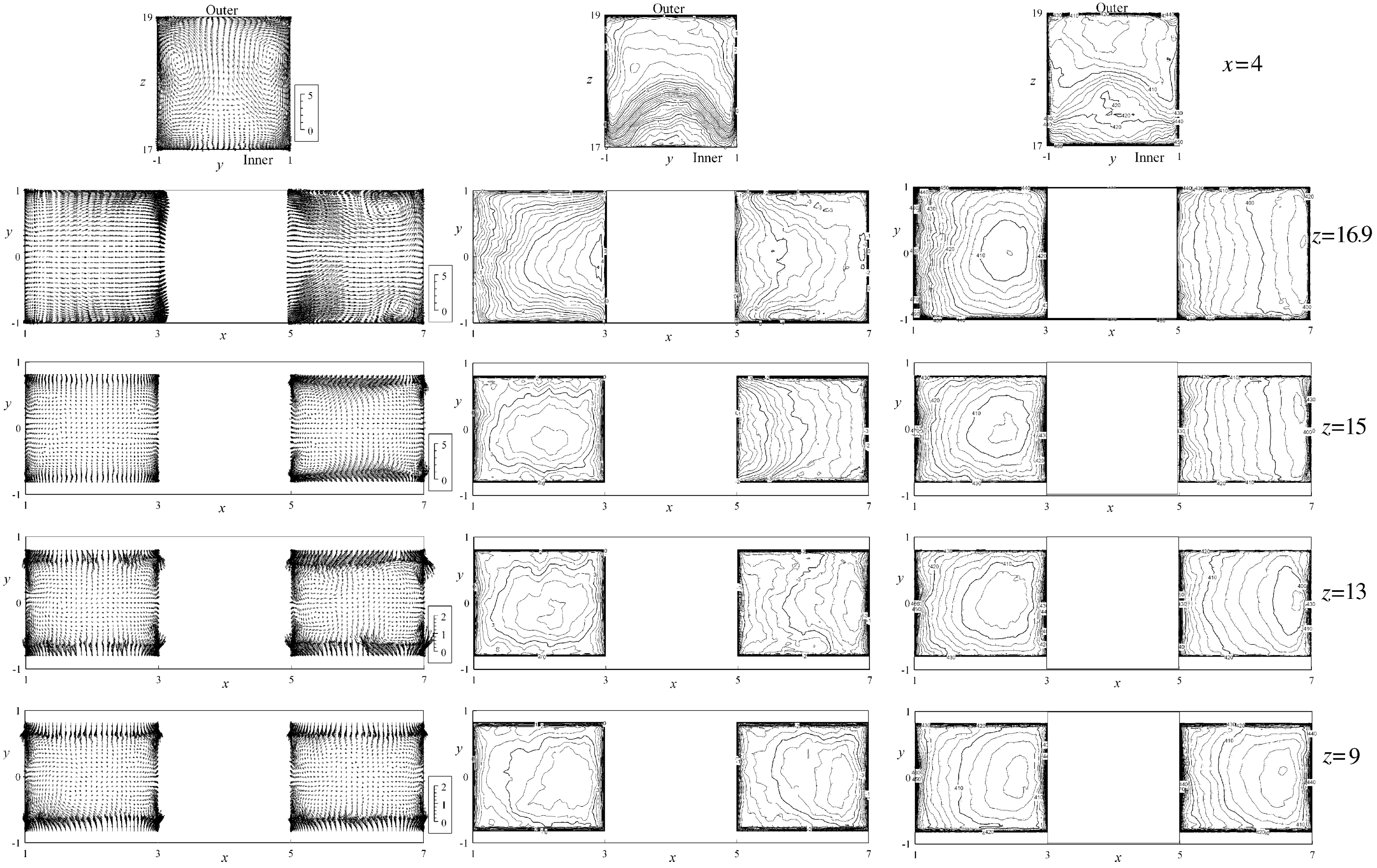

Fig. 7. Time-averaged velocity and temperature profiles in planes normal to duct-axis for $Ro_* = 0$ of 90° rib (left, middle, and right figures are for in-plane velocity vectors, plane-normal velocity component ($\overline{u}$ or $\overline{w}$), and temperature $\overline{\theta}$, respectively; from top to bottom, $x = 4$, $z = 16.9$, 15, 13, and 9. Isocontour lines are drawn by every 0.2 and 2 for ($\overline{u}$ or $\overline{w}$) and $\overline{\theta}$, respectively).

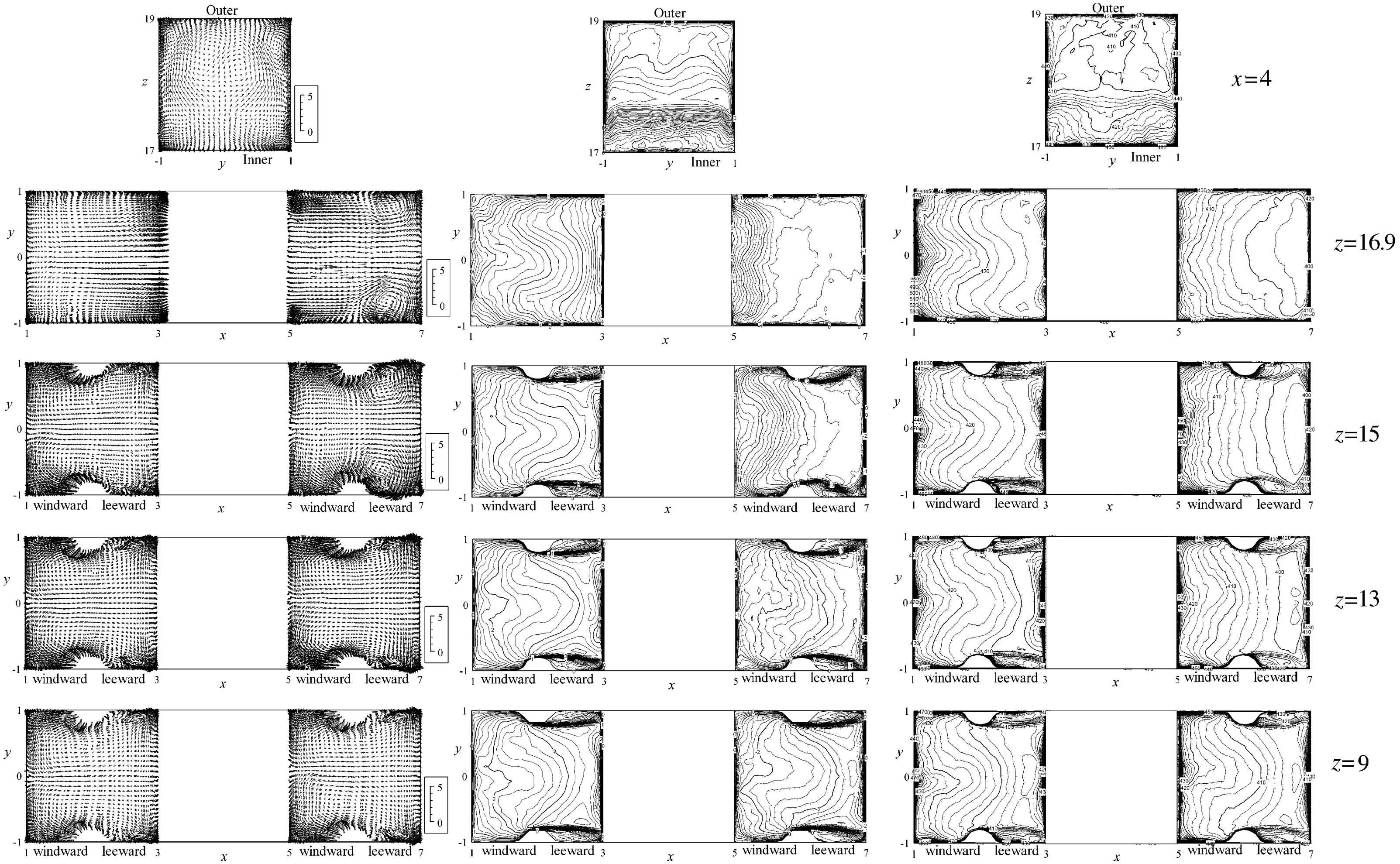

Fig. 8. Time-averaged velocity and temperature profiles in planes normal to duct-axis for $Ro_* = 0$ of 60° rib NP (legend is the same as that of Fig. 7).

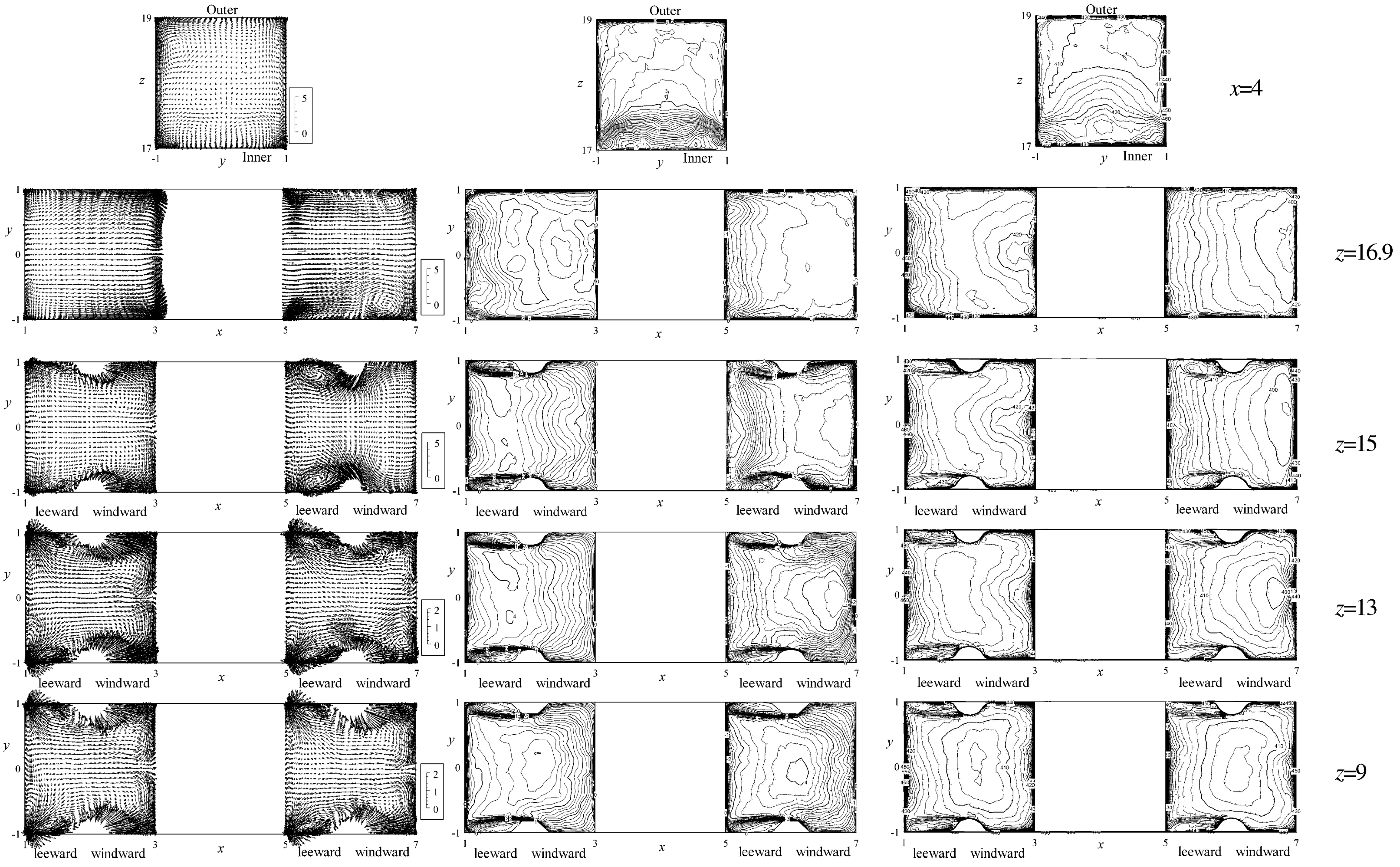

Fig. 9. Time-averaged velocity and temperature profiles in planes normal to duct-axis for $Ro_* = 0$ of 60° rib PN (legend is the same as that of Fig. 7).

are shown in Fig. 10 ($Ro_* = 1$ for the 60° rib NP). In this study, the trailing and leading walls of the first straight pass correspond to the pressure and suction surfaces, respectively, and opposite relation holds in the second straight pass. The pressure and suction surfaces are defined with respect to the Coriolis induced secondary flow, which impinges onto the pressure surface. In Fig. 10, the pressure surface shows the higher Nusselt number and the larger variation of the wall shear stress. In the turn A, the high heat transfer area on the leading wall is extended and intensified, and that on the trailing wall is separated in two regions: around the first inner corner and the second outer corner. The Nusselt number on the outer wall in the turn is intensified and slightly shifted to the trailing wall side. After the turn, the high heat transfer area is divided into two parts on the outer wall. The tendency was common for the 90° rib and the 60° rib PN cases (figures are not shown).

For the higher Ro_* of Figs. 11–13 ($Ro_* = 2$), the reverse flow area recognized by the negative wall shear

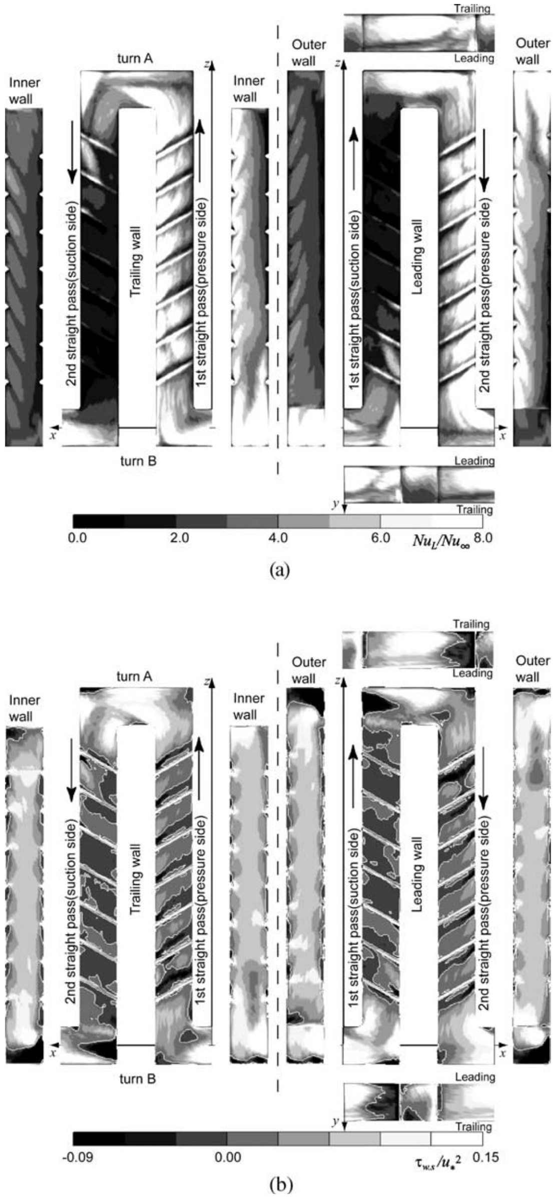

Fig. 10. Time-averaged profiles of (a) Nusselt number and (b) streamwise component of wall shear stress (60° rib NP, $Re_* = 1000$, $Re_m = 3447$, $Ro_* = 1$, and $Ro_m = 1.16$).

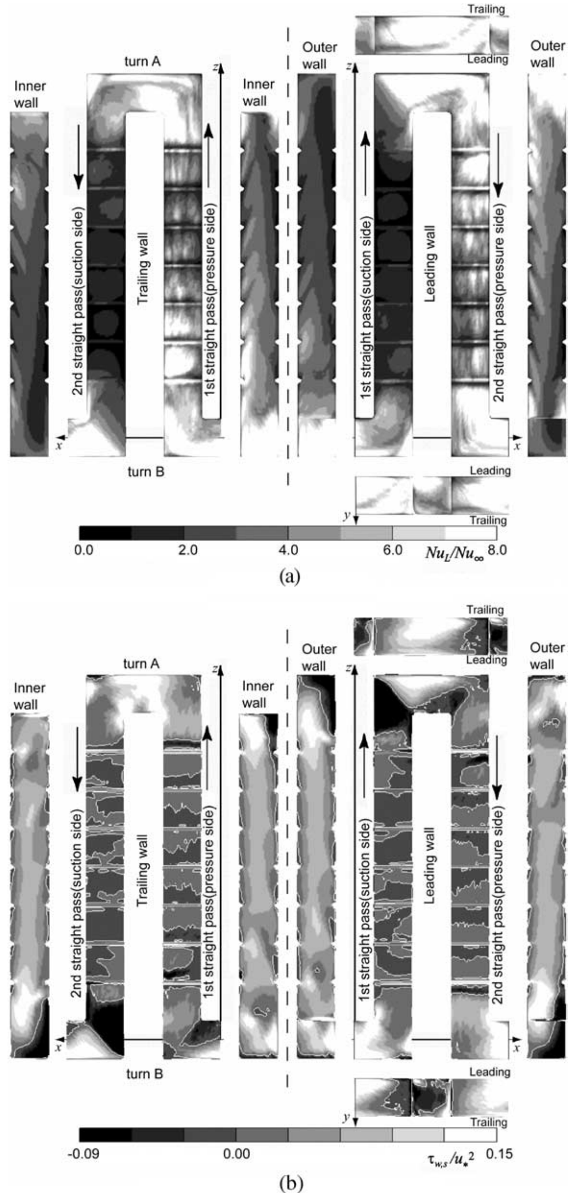

Fig. 11. Time-averaged profiles of (a) Nusselt number and (b) streamwise component of wall shear stress (90° rib, $Re_* = 1500$, $Re_m = 3671$, $Ro_* = 2$, and $Ro_m = 3.27$).

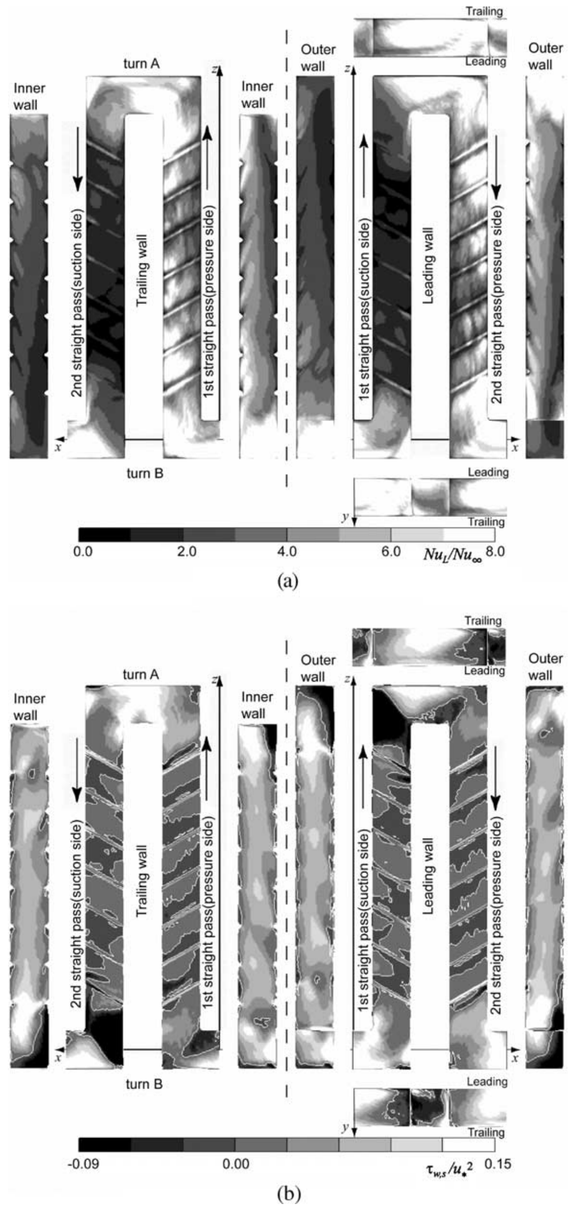

(a)

(b)

Fig. 12. Time-averaged profiles of (a) Nusselt number and (b) streamwise component of wall shear stress (60° rib NP, $Re_* = 1500$, $Re_m = 3772$, $Ro_* = 2$, and $Ro_m = 3.18$).

stress becomes larger at the turn entrance on the leading wall following the suction surface of the first straight pass. As compared to $Ro_* = 1$ case, the heat transfer on the pressure surface is deteriorated in the latter half of the straight pass. Alternating flow separation every two rib-pitches is observed on the suction surfaces in the 60° rib cases (Figs. 12(b) and 13(b)).

Fig. 14 shows the duct-axial variation of the transversely averaged Nusselt number for the 60° rib NP case.

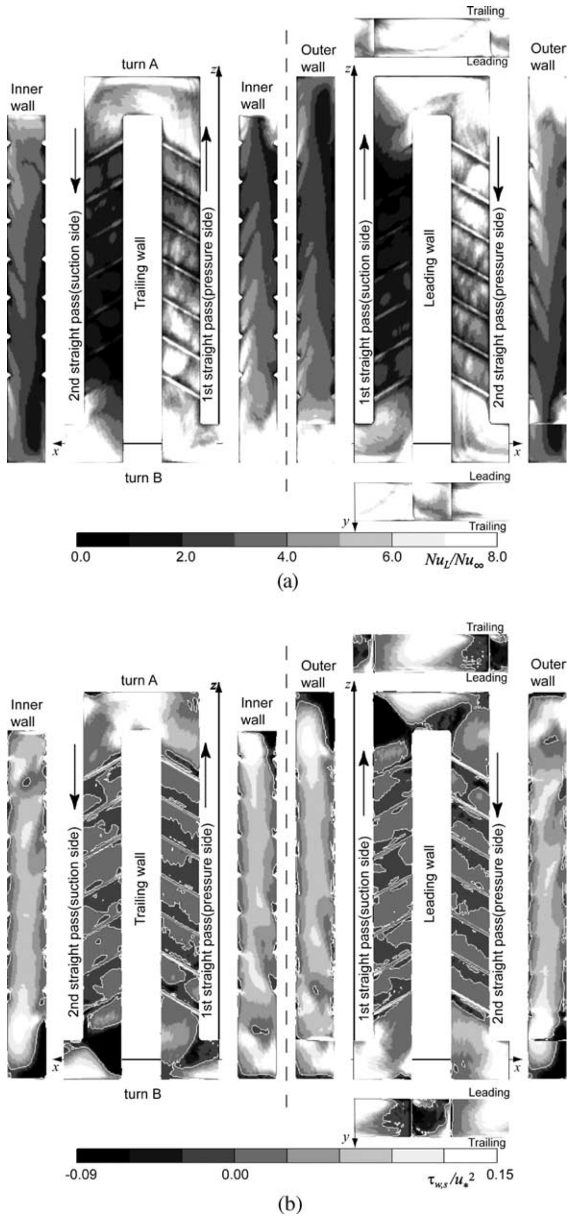

(a)

(b)

Fig. 13. Time-averaged profiles of (a) Nusselt number and (b) streamwise component of wall shear stress (60° rib PN, $Re_* = 1500$, $Re_m = 3695$, $Ro_* = 2$, and $Ro_m = 3.25$).

The transverse average was taken in the ξ direction, and therefore the averaging direction was aligned to the ribs. The thin, middle, and thick line widths correspond to $Ro_* = 0$, 1, and 2, respectively. Though figures are not shown, the following tendencies are also observed in the other two rib arrangements: quick development of periodic high heat transfer on and between the ribs, higher heat transfer in the turn for the higher Ro_* and the suppressed heat transfer for the increase of Ro_* from

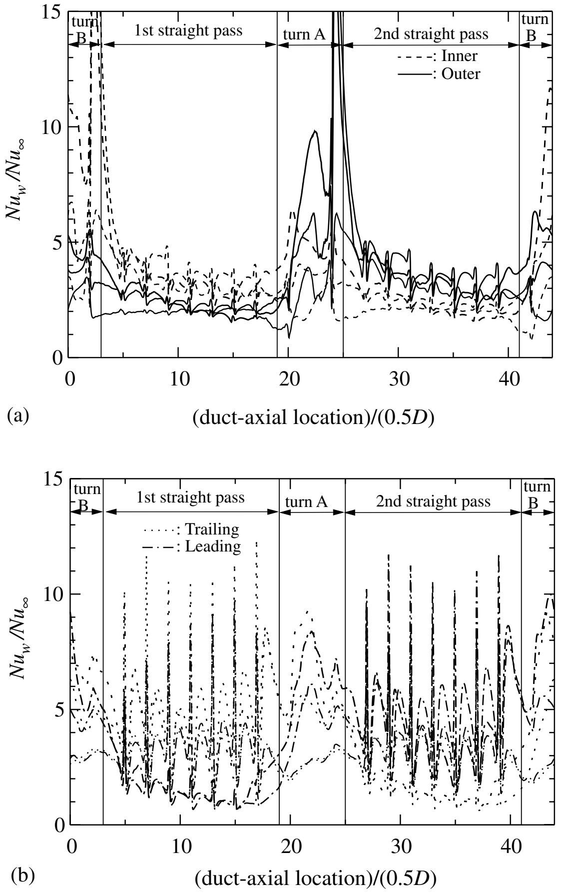

Fig. 14. Transversely averaged Nusselt number variation in the duct-axial direction for 60° rib NP case (thin, middle, and thick lines are for $Ro_* = 0$, 1, and 2, respectively). (a) Inner and outer walls, (b) leading and trailing walls.

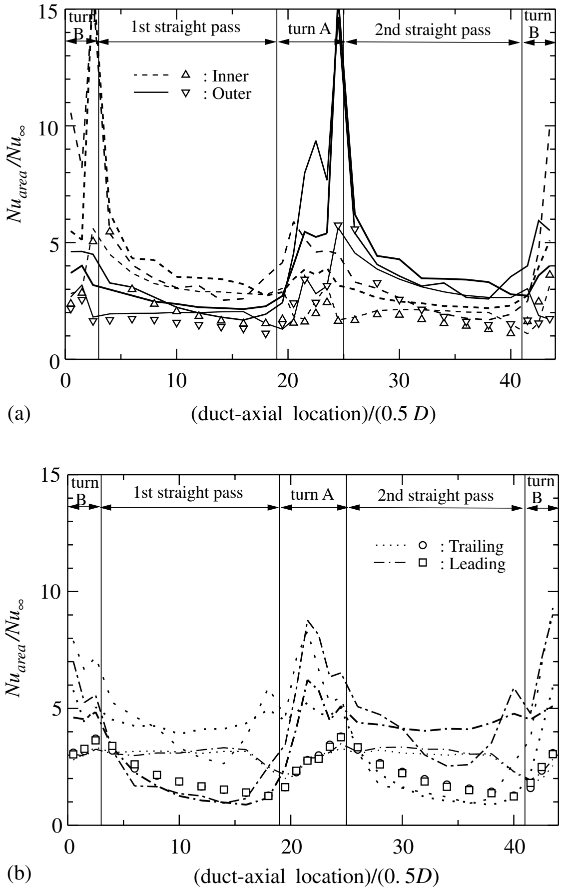

Fig. 15. Area-averaged Nusselt number variation in the duct-axial direction for 60° rib NP case (area average was performed in transverse and duct-axial directions with duct-axial pitch of D; thin, middle, and thick lines are for $Ro_* = 0$, 1, and 2, respectively; symbols are for stationary smooth channel results of Murata and Mochizuki [26]). (a) Inner and outer walls, (b) leading and trailing walls.

1 to 2 in the straight pass (especially in the latter half). The heat transfer between the ribs of the 60° rib NP arrangement becomes even lower than that of the stationary case in the middle of the straight pass on the pressure surface. In the previous experiments [11], the similar tendency was observed: the pressure-surface heat transfer dependency on the rotation number was not monotonic in the second pass after the turn, and the heat transfer decreased as the rotation number increased in some rotation number range.

Fig. 15 shows the duct-axial variation of the area-averaged Nusselt number, Nu_{area}, for the 60° rib NP case. In order to show the approximate tendency, the area average was taken with the pitch of D in the duct-axial direction for each wall in addition to the transverse average. The inner and outer wall results are shown in (a), and the leading and trailing wall results are in (b). The thin, middle, and thick line widths correspond to $Ro_* = 0$, 1, and 2, respectively. For comparison, the stationary smooth channel results [26] are also plotted in the figures. When the stationary rib-roughened case (thin lines) is compared with the smooth channel result (symbol), the heat transfer enhancement is seen on the rib-roughened walls, but the heat transfer profiles in the turn is not affected by the rib installation. It can be said that the heat transfer in the turn is dominated by the sharp-turn induced flow field in the stationary condition. These characteristics were common among three rib arrangements (figures not shown).

Fig. 16 show the time-averaged velocity and temperature in the plane normal to the local duct-axis for $Ro_* = 1$ of the 60° NP case. In the first straight pass, the Coriolis force forms the uniform streamwise velocity profiles in the x direction on the suction side and the high temperature fluid covers the area. This uniform

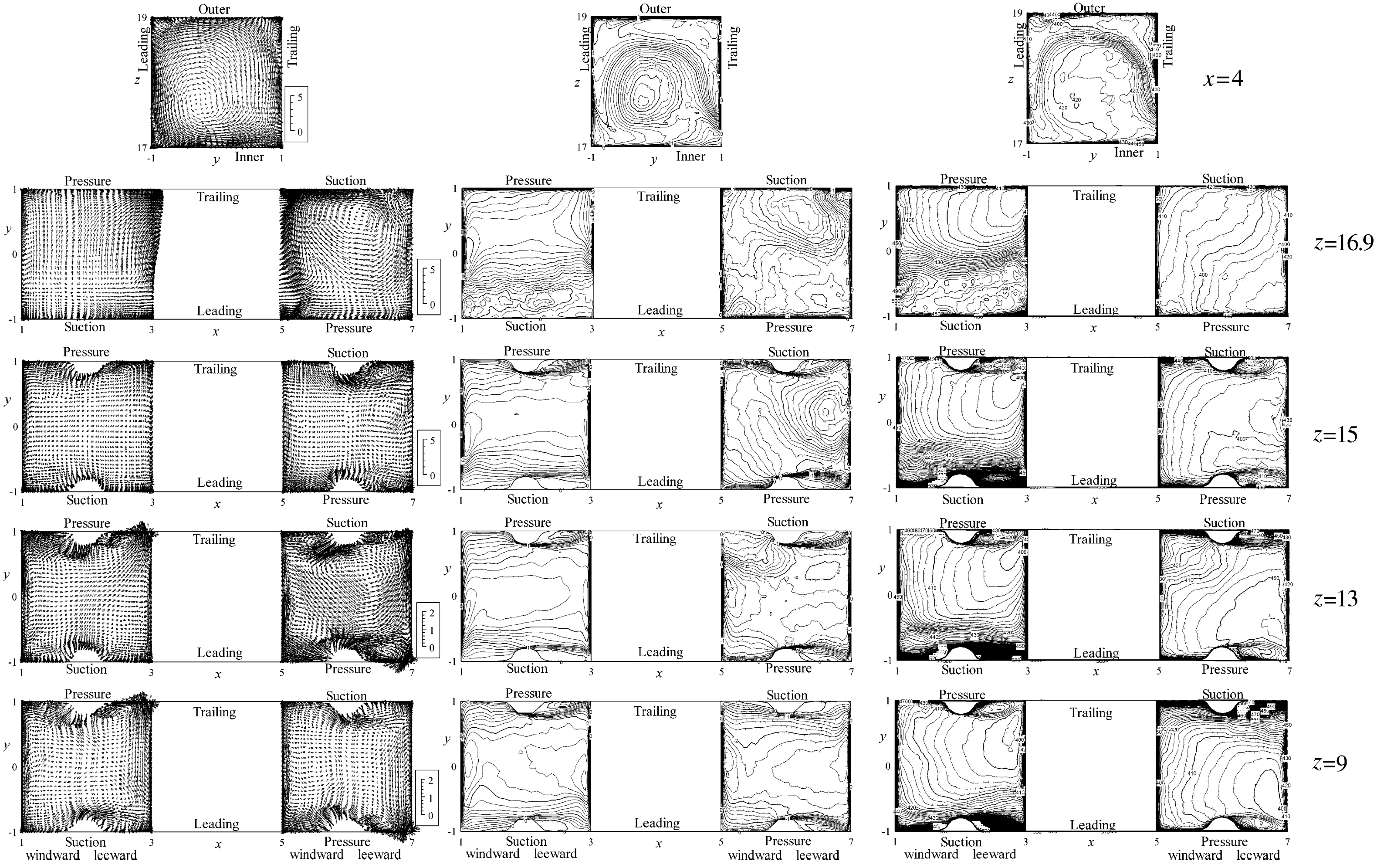

Fig. 16. Time-averaged velocity and temperature profiles in planes normal to duct-axis for $Ro_* = 1$ of 60° rib NP (legend is the same as that of Fig. 7).

profile is caused by the Taylor–Proudman effect [39] due to the balance between the pressure gradient and the Coriolis force that does not have a component in the x direction. In the y–z mid-plane of the turn (top figure of Fig. 16), the high momentum flow on the trailing side induces a dominating vortex that rotates in the counter-clockwise direction in the figure. Due to this strong vortex, the high momentum and low temperature fluid on the trailing side is transported to the leading side. At this y–z mid-plane, the reverse flow that located on the inner wall in the stationary condition (top figure of Fig. 8) shifts its location to the central region due to the strong vortex. After the turn, the strong vortex dominates at the turn outlet and at $z = 15.0$, but then the Coriolis force reverses the rotating direction of the vortex at $z = 13.0$.

For the higher rotation speed of $Ro_* = 2$ for the 60° rib NP case (Fig. 17), in the first straight pass, the uniformity of $\overline{w}$ profile are intensified. In the second straight pass of Fig. 17, due to the high rotation speed, the recovery of the $\overline{w}$ profile from that disturbed by the sharp turn to that uniform in the x direction seems quicker as compared to Fig. 16 of $Ro_* = 1$. When this intensified uniform profile appears, the turbulent kinetic energy becomes very low even on the pressure side as shown in Fig. 18, and this is the reason for the deteriorated heat transfer for $Ro_* = 2$ on the pressure surface of the straight pass as seen in Figs. 11–15. In Fig. 17, the profiles in the turn mid-plane ($x = 4$) and the turn exit ($z = 16.9$) were similar among the three rib arrangements (figures not shown). The alternating flow behavior as mentioned in Figs. 12 and 13 is observed in the alternating secondary flow direction for $z = 16.9$, 15, and 13 of Fig. 17. The alternating profile was also observed in the smooth channel case of $Ro_* = 2$ [26], and therefore for the high rotation speed the alternating flow field can be a stable solution in the present geometric configuration.

Fig. 19 shows the Colburn's j factor and the friction factor, f. The j and f factors are normalized by using j_∞ calculated from Nu_∞ in Eq. (11) and f_B in the following Blasius equation:

$$f_B = 0.079 Re_m^{-0.25} \tag{12}$$

The same results are summarized in Table 1 in order to show the increase percentage due to the channel rotation. In addition to the f factor, in order to isolate the sharp-turn effect on the pressure loss, the following turn pressure loss coefficient, K, is also plotted in Fig. 19 [40]:

$$K = \frac{\Delta p_{\text{turn}}}{\frac{1}{2}\rho U_m^2} \tag{13}$$

Here, Δp_{turn} is the pressure loss associated with the turn A, and it is calculated by linearly extrapolating the area-averaged wall-pressure profile at the central region of the first and second straight passes in the direction toward the turn inlet and outlet locations at $z = 17$ (see Fig. 2) [40]. In the stationary condition, the f factor is more sensitive to the rib arrangement than the j factor. The f factor is also very sensitive to the introduction of the channel rotation, and the 60° rib PN shows about 300% increase for $Ro_* = 2$ as compared to the stationary case; on the contrary, the j factor is relatively insensitive to the channel rotation and shows only about 15% increase for $Ro_* = 2$ in the 60° rib PN case. The effect of the duct rotation seems to be very high in the smooth duct case, and the duct rotation makes the f and j factors comparable to the rib-roughened cases. For the turn pressure loss coefficient, K, of the stationary condition, the 60° rib PN case gives the smallest value, and it is even smaller than the smooth channel case. Similarly to the f factor, K is very sensitive to the introduction of the channel rotation. Among the three rib arrangements, the 60° rib PN case is the most sensitive to the channel rotation in both the f and j factors. The friction factor in the rotating condition is very valuable data because the reliable experimental data of the pressure loss in the rotating condition is not available. The principle of the pressure gauge (usually a strain gauge) does not work properly in the rotating condition due to the high centrifugal force.

In order to further examine the heat transfer efficiency taking pressure loss into account, the heat transfer efficiency index, η_{eff}, was calculated by using the following equation [41]:

$$\eta_{\text{eff}} = \frac{St/St_{\text{smooth,stationary}}}{(f/f_{\text{smooth,stationary}})^{1/3}} \tag{14}$$

As explained in [41], η_{eff} is the index of the heat conductance for equal pumping power and heat transfer surface area. As shown in Fig. 20, for the stationary condition, the 60° rib PN case has the highest η_{eff}. On the other hand, when the channel rotates, η_{eff} decreases for all the rib arrangements, and that of the rib-roughened channels becomes lower than the smooth channel case for $Ro_* = 2$. In the rotating condition, the 60° rib NP and PN cases have the same level of η_{eff}.

4. Conclusions

The large eddy simulation of the two-pass square rib-roughened channel with the 180° sharp turns was performed changing rib arrangements for both the stationary and rotating conditions. From the numerical results the following conclusions were drawn.

In the stationary condition, the high heat transfer in and after the turn was similar to each other and to the smooth channel case. It can be said that the heat transfer in the sharp turn was dominated by the sharp-turn

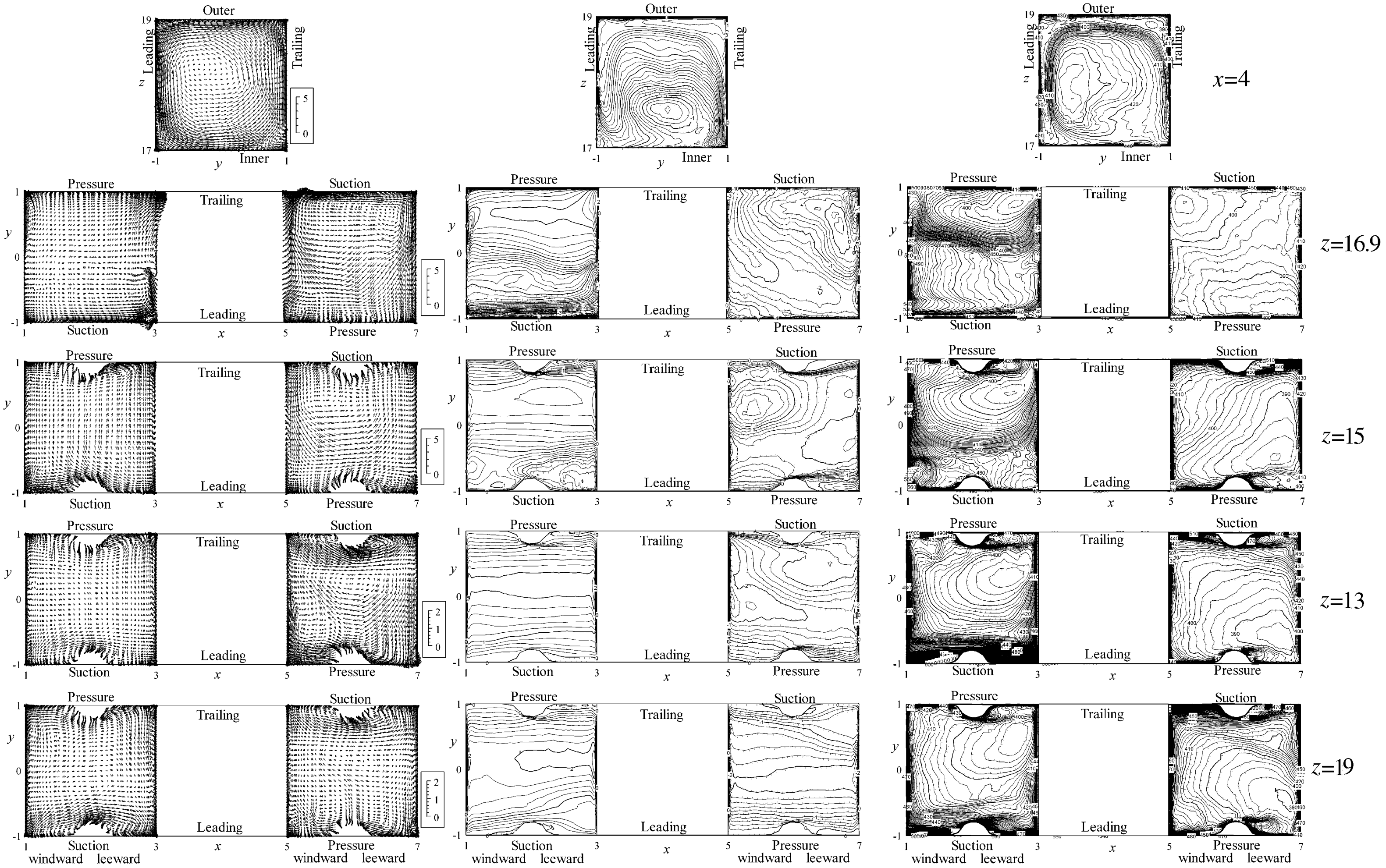

Fig. 17. Time-averaged velocity and temperature profiles in planes normal to duct-axis for $Ro_* = 2$ of 60° rib NP (legend is the same as that of Fig. 7).

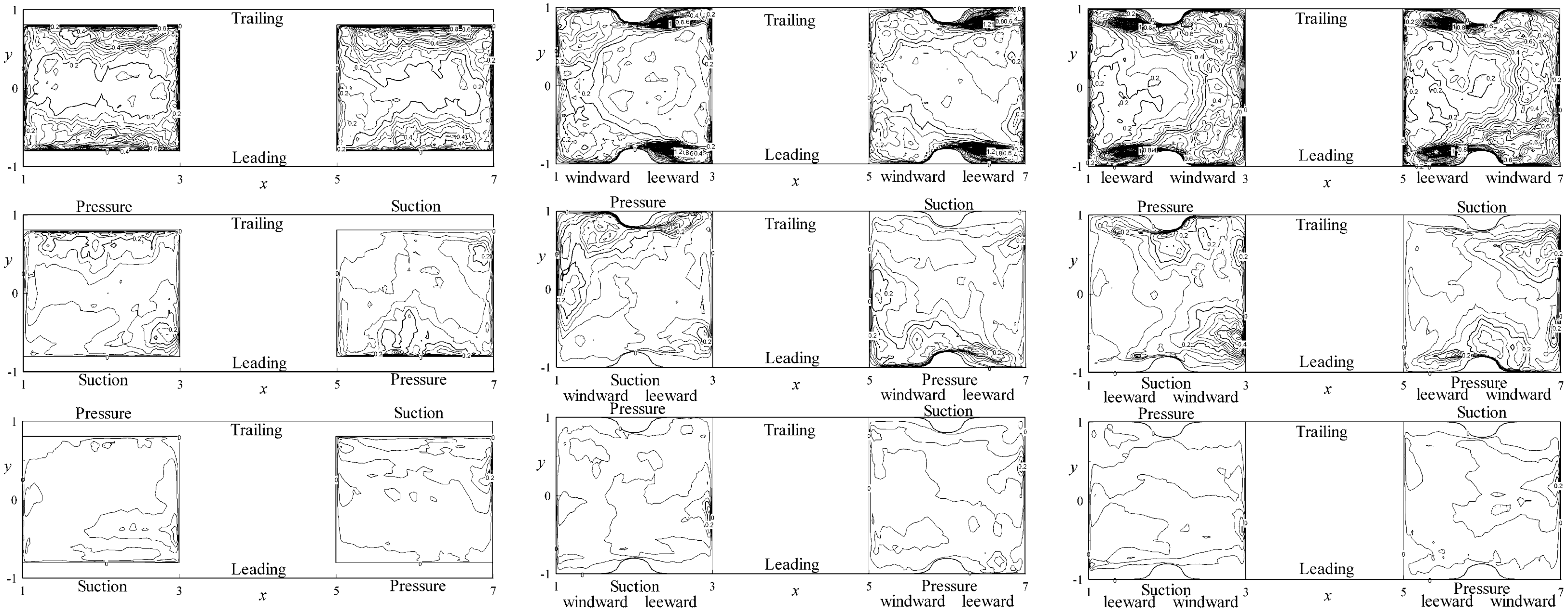

(a) 90deg rib (b) 60deg rib NP (c) 60deg rib PN

Fig. 18. Turbulent kinetic energy profile in plane normal to duct-axis at middle of straight pass ($z = 9$) (top, middle, and bottom figures are for $Ro_* = 0$, 1, and 2, respectively; isocontour lines are drawn by every 0.04).

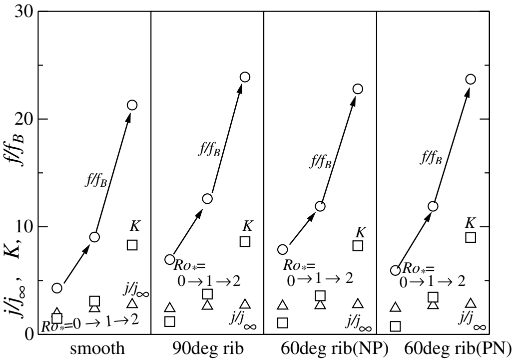

Fig. 19. Effect of channel rotation on f, K, and j factors (smooth channel results are from Murata and Mochizuki [26]).

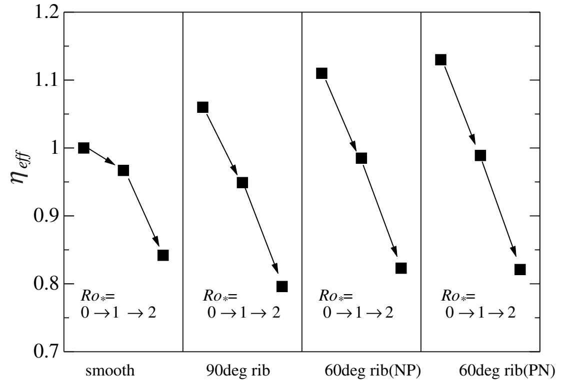

Fig. 20. Effect of channel rotation on heat transfer efficiency index (smooth channel results are from Murata and Mochizuki [26]).

induced flow field. In the rib-roughened straight pass, the flow quickly develops in a few rib-pitches. The angled-rib orientation affected the heat transfer in the straight pass due to the redevelopment of the secondary flow after the sharp-turn disturbance, and the NP arrangement gave higher heat transfer on the rib-roughened walls than the PN arrangement.

When the channel was rotated, the flow and heat transfer in the turn was mainly dominated by the sharp-turn and the Coriolis force effects. For the highest rotation number case of this study ($Ro_* = 2$), the Nusselt number on the pressure surface of the straight pass was deteriorated due to the suppressed turbulence, and an interesting alternating flow behavior was observed.

The friction factor was more sensitive to both the rib arrangement and the channel rotation than the channel averaged Nusselt number, and for $Ro_* = 2$ the friction factor of the 60° rib PN arrangement showed about 300% increase as compared to the stationary case. On the contrary, the channel averaged Nusselt number was insensitive to the channel rotation, and it showed, at most, only 15% increase as compared to the stationary case. The heat transfer efficiency index taking pressure loss into account gave the highest value for the 60° rib PN arrangement in the stationary condition, and in the rotating condition the 60° rib NP and PN arrangements gave almost the same efficiency.

References

[1] J.-C. Han, Recent studies in turbine blade cooling, CD-ROM Proc. 9th Int. Symp. Transport Phenomena Dyn. Rotat. Mach., Honolulu, Hawaii, US, Invited Lecture, 2002, pp. 1–16.

[2] A. Murata, S. Mochizuki, M. Fukunaga, Detailed measurement of local heat transfer in a square-cross-section duct with a sharp 180-deg turn, Heat Transfer 1994, Proc. Int. Heat Transfer Conf., Brighton, GB, vol. 4, 1994, pp. 291–296.

[3] S. Mochizuki, A. Murata, M. Fukunaga, Effects of rib arrangements on pressure drop and heat transfer in a rib-roughened channel with a sharp 180° turn, Trans. ASME, J. Turbomach. 119 (1997) 610–616.

[4] P.R. Chandra, J.C. Han, S.C. Lau, Effect of rib angle on local heat/mass transfer distribution in a two-pass rib-roughened channel, Trans. ASME, J. Turbomach. 110 (1988) 233–241.

[5] M. Hirota, H. Fujita, A. Syuhada, S. Araki, T. Yoshida, T. Tanaka, Heat/mass transfer characteristics in two-pass smooth channels with a sharp 180-deg turn, Int. J. Heat Mass Transfer 42 (1999) 3757–3770.

[6] S.V. Ekkad, J.C. Han, Detailed heat transfer distributions in two-pass square channels with rib turbulators, Int. J. Heat Mass Transfer 40-11 (1997) 2525–2537.

[7] T.M. Liou, C.C. Chen, T.W. Tsai, Liquid crystal measurements of heat transfer in a 180° sharp turning duct with different divider thicknesses, CD-ROM Proc. 8th Int. Symp. Flow Visualization, Sorrento, Italy, 1998, pp. 71.1–71.9.

[8] T. Astarita, G. Cardone, Thermofluidynamic analysis of the flow in a sharp 180° turn channel, Expt. Thermal Fluid Sci. 20 (2000) 188–200.

[9] S.Y. Son, K.D. Kihm, J.-C. Han, PIV flow measurements for heat transfer characterization in two-pass square channels with smooth and 90° ribbed walls, Int. J. Heat Mass Transfer 45 (2002) 4809–4822.

[10] J.-C. Han, Y.-M. Zhang, K. Kalkuehler, Uneven wall temperature effect on local heat transfer in a rotating two-pass square channel with smooth walls, Trans. ASME J. Heat Transfer 115 (1993) 912–920.

[11] J.H. Wagner, B.V. Johnson, F.C. Kopper, Heat transfer in rotatingserpentine passages with smooth walls, Trans. ASME J. Turbomach. 113 (1991) 321–330.

[12] S. Mochizuki, J. Takamura, S. Yamawaki, W.-J. Yang, Heat transfer in serpentine flow passages with rotation, Trans. ASME J. Turbomach. 116 (1994) 133–140.

[13] J.A. Parsons, J.-C. Han, Y.-M. Zhang, Effect of model orientation and wall heating condition on local heat

transfer in a rotating two-pass square channel with rib turbulators, Int. J. Heat Mass Transfer 38-7 (1995) 1151–1159.

[14] B.V. Johnson, J.H. Wagner, G.D. Steuber, F.C. Yeh, Heat transfer in rotating serpentine passages with trips skewed to the flow, Trans. ASME J. Turbomach. 116 (1994) 113–123.

[15] S. Mochizuki, M. Beier, A. Murata, T. Okamura, Y. Hashidate, Detailed measurement of convective heat transfer in rotating two-pass rib-roughened coolant channels, ASME Paper, 96-TA-6 (1996).

[16] T.-M. Liou, C.-C. Chen, M.-Y. Chen, TLCT and LDV measurements of heat transfer and fluid flow in a rotating sharp turning duct, Int. J. Heat Mass Transfer 44 (2001) 1777–1787.

[17] B. Banhoff, U. Tomm, B.V. Johnson, I. Jennions, Heat transfer predictions for rotating U-shaped coolant channels with skewed ribs and with smooth walls, ASME Paper, 97-GT-162 (1997).

[18] Y.-L. Lin, T.I-P. Shih, M.A. Stephens, M.K. Chyu, A numerical study of flow and heat transfer in a smooth and ribbed U-duct with and without rotation, Trans. ASME J. Heat Transfer 123 (2001) 219–232.

[19] A. Huser, S. Biringen, Direct numerical simulation of turbulent flow in a square duct, J. Fluid Mech. 257 (1993) 65–95.

[20] S. Gavrilakis, Numerical simulation of low Reynolds number turbulent flow through a straight square duct, J. Fluid Mech. 244 (1992) 101–129.

[21] R.K. Madabhushi, S.P. Vanka, Large eddy simulation of turbulence-driven secondary flow in a square duct, Phys. Fluids A3-11 (1991) 2734–2745.

[22] A. Murata, S. Mochizuki, Effect of cross-sectional aspect ratio on turbulent heat transfer in an orthogonally rotating rectangular smooth duct, Int. J. Heat Mass Transfer 42 (1999) 3803–3814.

[23] J. Pallares, L. Davidson, Large eddy simulations of turbulent flow in a rotating square duct, Phys. Fluids 12-11 (2000) 2878–2894.

[24] A. Murata, S. Mochizuki, Large eddy simulation of turbulent heat transfer in an orthogonally rotating square duct with angled rib turbulators, Trans. ASME J. Heat Transfer 123 (2001) 858–867.

[25] A. Murata, S. Mochizuki, Effect of centrifugal buoyancy on turbulent heat transfer in an orthogonally rotating square duct with transverse or angled rib turbulators, Int. J. Heat Mass Transfer 44 (2001) 2739–2750.

[26] A. Murata, S. Mochizuki, Large eddy simulation of turbulent heat transfer in a rotating two-pass smooth square channel with sharp 180-deg turns, Int. J. Heat Mass Transfer 47 (2004) 683–698.

[27] M.E. Taslim, S.D. Spring, Effect of turbulator profile and spacing on heat transfer and friction in a channel, J. Thermophys. Heat Transfer 8-3 (1994) 555–562.

[28] G.J. Korotky, M.E. Taslim, Rib heat transfer coefficient measurements in a rib-roughened square passage, ASME Paper, 96-GT-356 (1996).

[29] M.E. Taslim, T. Li, D.M. Kercher, Experimental heat transfer and friction in channels roughened with angled, V-shaped, and discrete ribs on two opposite walls, Trans. ASME J. Turbomach. 118 (1996) 20–28.

[30] J.C. Han, J.S. Park, C.K. Lei, Heat transfer enhancement in channels with turbulence promoters, Trans. ASME. J. Eng. Gas Turbines Power 107 (1985) 628–635.

[31] S.V. Patankar, C.H. Liu, E.M. Sparrow, Fully developed flow and heat transfer in ducts having streamwise-periodic variations of cross-sectional area, Trans. ASME J. Heat Transfer 99 (1977) 180–186.

[32] T. Kajishima, T. Ohta, K. Okazaki, Y. Miyake, High-order finite-difference method for incompressible flows using collocated grid system, JSME Int. J. Series B 41-4 (1998) 830–839.

[33] C. Meneveau, T.S. Lund, W.H. Cabot, A Lagrangian dynamic subgrid-scale model of turbulence, J. Fluid Mech. 319 (1996) 353–385.

[34] P. Moin, K. Squires, W. Cabot, S. Lee, A dynamic subgrid-scale model for compressible turbulence and scalar transport, Phys. Fluids A3-11 (1991) 2746–2757.

[35] F.H. Harlow, J.E. Welch, Numerical calculation of time-dependent viscous incompressible flow of fluid with free surface, Phys. Fluids 8–12 (1965) 2182–2189.

[36] J. Kim, P. Moin, Application of a fractional-step method to incompressible Navier–Stokes equations, J. Comp. Phys. 59 (1985) 308–323.

[37] Y. Zang, R.L. Street, J.R. Koseff, A non-staggered grid, fractional step method for time-dependent incompressible Navier–Stokes equations in curvilinear coordinates, J. Comp. Phys. 114 (1994) 18–33.

[38] W.M. Kays, M.E. Crawford, Convective Heat and Mass Transfer, third ed., McGraw-Hill Inc., New York, 1993, p. 316.

[39] G.K. Batchelor, An Introduction to Fluid Dynamics, Cambridge Univ. Press, Ch, 1967, pp. 555–559.

[40] D.E. Metzger, C.W. Plevich, C.S. Fan, Pressure loss through sharp 180° turns in smooth rectangular channels, J. Eng. Gas Turbines Power 106 (1984) 677–681.

[41] D.L. Gee, R.L. Webb, Forced convection heat transfer in helically rib-roughened tubes, Int. J. Heat Mass Transfer 23 (1980) 1127–1136.